Journal of Thermal Science Vol.21, No.3 (2012) 286–294

DOI: 10.1007/s11630-012-0546-1 **Article ID: 1003-2169(2012)03-0286-09**

Conjugate Heat Transfer Characterization in Cooling Channels

Beni Cukurel, Tony Arts, and Claudio Selcan

von Karman Institute for Fluid Dynamics – Turbomachinery Department, Chaussée de Waterloo, 72, B-1640, Rhode-St-Genèse, Belgium

Cooling technology of gas turbine blades, primarily ensured via internal forced convection, is aimed towards withdrawing thermal energy from the airfoil. To promote heat exchange, the walls of internal cooling passages are lined with repeated geometrical flow disturbance elements and surface non-uniformities. Raising the heat transfer at the expense of increased pressure loss; the goal is to obtain the highest possible cooling effectiveness at the lowest possible pressure drop penalty. The cooling channel heat transfer problem involves convection in the fluid domain and conduction in the solid. This coupled behavior is known as conjugate heat transfer. This experimental study models the effects of conduction coupling on convective heat transfer by applying iso-heat-flux boundary condition at the external side of a scaled serpentine passage. Investigations involve local temperature measurements performed by Infrared Thermography over flat and ribbed slab configurations. Nusselt number distributions along the wetted surface are obtained by means of heat flux distributions, computed from an energy balance within the metal domain. For the flat plate experiments, the effect of conjugate boundary condition on heat transfer is estimated to be in the order of 3%. In the ribbed channel case, the normalized Nusselt number distributions are compared with the basic flow features. Contrasting the findings with other conjugate and convective iso-heat-flux literature, a high degree of overall correlation is evident.

Keywords: conjugate heat transfer, turbine cooling channel, convection, infrared thermography

Introduction

Investigating an internal cooling channel model (numerically or experimentally), the reproduced thermal boundary conditions should resemble the engine environment. If this is not the case, the modeling of the heat transfer process may be inaccurate. Most prior literature in this field does not address the issue of thermal boundary condition influence. In purely convective studies, where uniform temperature or uniform heat flux is imposed along the wetted surface, the thermal boundary conditions are clearly not realistic. Hence, the effect of the thermal history of the flow field is neglected. On the contrary, in conjugate heat transfer theory, where the effects of solid domain conduction are coupled with the convection over the surface, no constraint is enforced at the solid-fluid interface, except thermal equilibrium and heat flux continuity. The conjugate heat transfer analysis presents an opportunity to accurately model real engine conditions.

Perelman defines the conjugate heat transfer as the problem of generally unknown temperature and heat flux distributions at the solid-fluid interface, established by the coupled solving of the thermo-fluid dynamic equations in the fluid and the energy equation in the solid [1]. Analytical solutions of conjugate problems rely on me-

Received: December 2012 Tony Arts: Professor
Support financially by the Air Force Office of Scientific Research (AFOSR), Grant FA8655-08-1-3048

Nomenclature

Bi	$h\,d/k_s$ [Biot Number]	Re	Reynolds number
D_h	Channel hydraulic diameter	T	Temperature
EF	Nu/Nu_0 [Enhancement Factor]	ΔT	T_s-T_∞ [temperature head]
h	$q/\Delta T$ [Heat transfer coefficient]	x	Axial Distance
H	Rib height	y	Lateral Distance
k	Thermal conductivity	z	Longitudinal Distance
K	k_s/k_f	**Subscripts**	
Nu	$h\,D_h/k_f$ [Nusselt number]	f	fluid
Nu_0	$0.0243Re^{0.8}Pr^{0.4}$	s	solid
Pr	Prandtl number	∞	freestream

thods that determine the heat transfer from arbitrary non-isothermal surfaces [2]. Fundamental analytical studies have been presented by Luikov and Aleksashenko [3], who solved the heat transfer problem for the case of an incompressible laminar fluid flow along a flat plate with applying a uniform temperature distribution at the bottom surface of the solid. Quantifying the thermal resistance ratio of the plate to that of the laminar boundary layer, Luikov [4] introduced the Brun number as a conjugation criterion.

Considering the scarcity of experimental data geared towards conjugate heat transfer, the present work can be considered a baseline benchmark case for numerical validation. Uniform heat flux boundary condition is applied at the external side of a geometrically scaled test section of an internal cooling channel with flat and ribbed walls; surface temperature distributions are measured via Infrared Thermography. This study exemplifies the pioneering experimental efforts to include the effects of conduction coupling in forced convection applications.

Flow in a Ribbed Cooling Channel

The relatively simple geometry of rib roughened internal cooling passages is misleading in a sense that the employed step disturbance elements introduce a number of complex secondary flow features into the mean stream, Fig. 1, [5].

Approaching from the right hand side of the figure the fluid enters the test section and encounters the rib. The stream experiences a strong deviation imposed by the obstacle, forcing it to adapt to the decreased channel cross section. It is accelerated in order to pass the rib and subsequently experiences an expansion further downstream, as the cross sectional area abruptly increases due to the backward-facing step. This is also supported by the large pressure drop located in the proximity of the rib [6].

The periodic behavior of consecutive acceleration in the vicinity of the obstacle and deceleration of the fluid in the inter-rib spacing is one most dominant aspect of the flow field in rib-roughened channels. Since the fluid flow is not able to follow the abrupt changes of the surface, it is the sudden enlargement of the channel after passing the perturbator which causes the flow to separate from the surface. A free shear layer is formed upon the interaction between the separated flow and the reverse flow in the recirculation region downstream of the rib, Fig. 1.

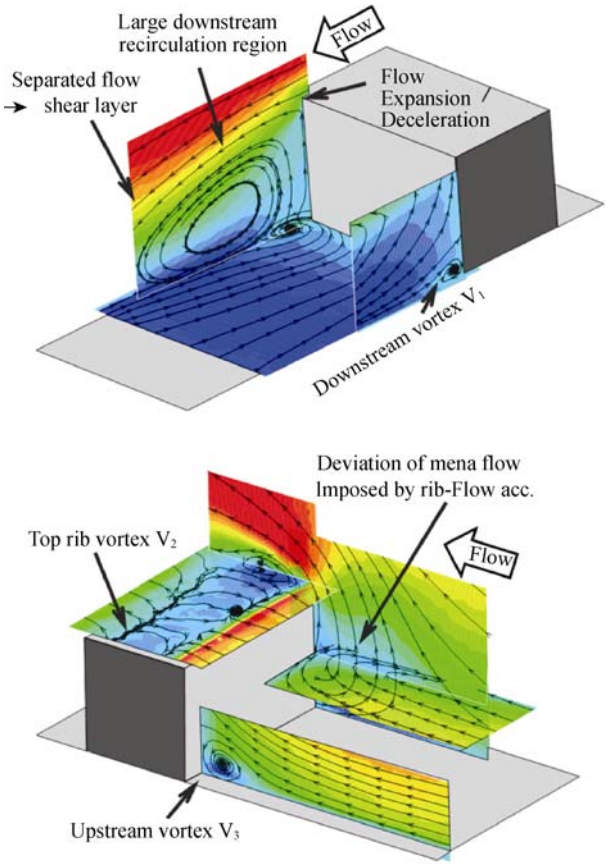

Fig. 1 Visualization of the Ribbed Channel Flow Field [5]

Apart from this recirculation region, the flow field exhibits a local separated flow region V_2 on top of the perturbator as well as a small vortex V_1 in the downstream

corner between the rib and the channel bottom wall, as indicated by Rau et al. [6].

Further downstream, the mean flow passes the rib and the subsequent recirculation zone, and at the reattachment region, there exists an impingement towards the channel wall. Once the flow reattaches and aligns with the channel wall, the boundary layer redevelops and grows within the inter-rib spacing, until it approaches the next turbulator. The stream strongly impinges on the front surface of the rib, and the local vorticity gives rise to the vortex structure V_3 [5].

Ribbed Channel Geometric Similarity

The important geometric scales for flow development inside rib roughened cooling channels are aspect ratio, blockage factor, rib pitch to height ratio, rib angle of attack, rib shape and profile and number of ribbed channel walls. The blockage ratio is of major importance for the flow behavior in a rib-roughened channel. The majority of studies on heat transfer enhancement in literature involve configurations characterized by noteworthy small blockage or rib height to hydraulic diameter ratios with H/D_h = [0.02-0.08]. In the present work, the test section geometrical dimensions are similar to the former studies carried out in this field at Von Karman Institute. The geometric parameters of the square channel are selected to yield a blockage ratio of 0.3, rib pitch to height ratio of 10, and angle of attack of 90°.

The chosen configuration combines the setting of a standard reference case, squared cross section, with a high blockage ratio of the channel. It results in a particularly complex flow behavior with high levels of turbulence and a substantially three-dimensional flow character [5]. Therefore it is suitable for a fundamental analysis of the rib-roughened channel flow. From the perspective of aerodynamic similarity to engine conditions, experiments are conducted at Re= 40,000. For conjugate heat transfer considerations, engine representative Biot number, Bi, and solid to fluid thermal conductivity ratio (K) are used, 1 and 600 respectively. At such a high thermal conductivity ratio and Biot number being in the order of unity, considering both thermal and convective resistances are of the same order, the conjugate effects are expected to be augmented.

Experimental Facility

The facility is a simplified model of an internal cooling blade channel that is scaled up by a factor of 15. It consists of three pieces such as the inlet, test and exit sections and each section has a cross-sectional dimension of 75x75mm, with longitudinal dimension of 1400mm, 1260mm, 800mm respectively. The basic schematic of the test section can be found in Fig. 2.

The test section consists of several components, where at the base of the channel a flat slab made of Steel AISI304 rests. The thickness of the slab (25mm) has been chosen such that it respects the similarity with the serpentine channels of a turbine blade where the Biot number is approximately equal to 1.

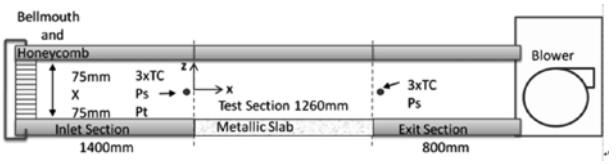

Fig. 2 Schematic of the Experimental Facility

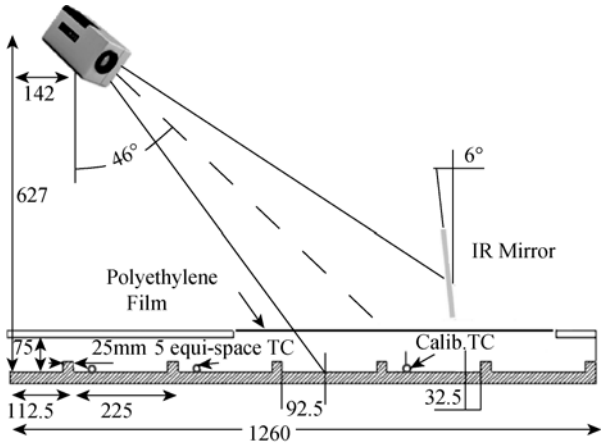

Fig. 3 Ribbed Slab Test Section and Camera [mm]

The steel slab is painted black with uniform highly emissive layers of Nextel Primer 5523 and Nextel Suede Coating 428-26, by means of an airbrush. The black coating is mat, soft and due to diffuse reflection the surface is non-dazzling. The end finish is found to be suitable for infrared measurements due to its black-body like behavior, albeit the camera is calibrated for the specific setup and the performance of the black paint is merely a matter of measurement quality. At the external side of the bottom wall, the slab is heated by means of a 25μm thick Inconel sheet which is powered by a 16V-150A DC power supply. The current is dissipated as thermal energy by the Joule effect and is conducted away by the parts in contact. Inconel provides uniform heat flux across the applied area and retains strength over a wide range of temperatures.

The slab is instrumented with 14 T-type thermocouples, held in place by Omega OB-101 thermally conductive, electrically insulating paste, applied to 3mm holes drilled in the metallic slab at several locations along the slab. The thermocouples are located 0.5 mm away from the surface of the slab, and considering the Biot number,

approximately 10^{-3}, for this characteristic length, it is observed that the temperatures measured at the thermocouple bead locations are equivalent to surface measurements.

The FLIR SC3000 infrared camera (with a total resolution and thermal sensitivity of 240x320 pixels, 0.02°K respectively) is located at 46° from the vertical, Fig. 3. Since the radiation exchange of surfaces are linearly proportional with the view factor, this configuration is selected to provide a good compromise for pixels on both the vertical and horizontal surfaces. The downstream face of the rib, along with the rib-shadowed portion of the inter-rib space is observed via a Newport 75K00ER.3 mirror, featuring a reflectance in the order of 95 percent in the 8-9 micron range of the camera.

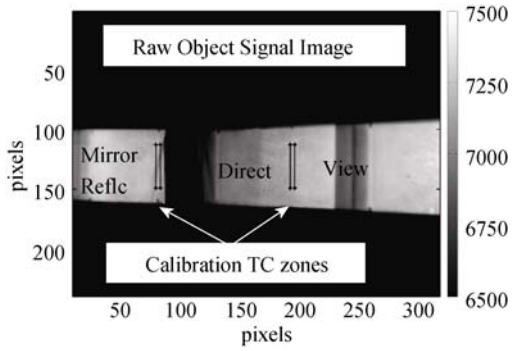

Fig. 4 Raw IR Image Object Signal

Calibration Methodology

Infrared thermography for surface temperature interrogation is based on an accurate calibration of the object signal acquired by the IR observation camera against the test surface temperature.

The infrared radiation, emitted by the model and its surroundings, is absorbed by the photon-detectors of the infrared camera for which the signal intensity is a function of slab area and temperature as well as relative orientation of the surfaces. The irradiation is subsequently converted to electrical signals, "object signal", at each pixel.

In the case of the ribbed slab configuration, due to the three-dimensionality of the surface, the application of a pixel-by-pixel calibration is not possible, since it demands a well quantified temperature distribution on the test surface, which is unfeasible to attain. Hence, in the present investigation, a single point calibration procedure is utilized. This methodology is based on the assumption that the slope of the calibration curve is constant for all the pixels of the image, which enables the use of a single curve found at the reference point, with well known temperature, to retrieve the complete temperature map across the test surface.

Acquisition of a series of reference temperature levels, which span the bandwidth exhibited during the experiment, yield a calibration curve correlating camera signals with thermocouple readings.

Figure 4 presents the raw object signal as acquired by the camera during data acquisition. The superimposed rectangular regions (calibration reference zones) indicate the location of the thermocouples embedded into the slab, as observed directly and reflected from the mirror. Considering the large difference in view factors of the direct and mirror reflected portions of the image, independent in-situ calibrations are performed. For the pixels outside of the calibration zone, the out of focus effects are compensated by acquiring infrared images under conditions where the slab is at uniform ambient temperature; and the deviation of object signal from the reference zone is utilized as a local bias shift.

Image Processing

All segments of the image are transformed independently by a perspective transformation, which uses bicubic interpolation, and are projected onto a plane, Fig. 5. Since this procedure is conducted independently on different regions of the geometry and the perspective of the camera varies significantly along the image, it is not possible to define a true uniform scale factor. Nevertheless, the mean scale factor is calculated to be 2.64 pixels/mm.

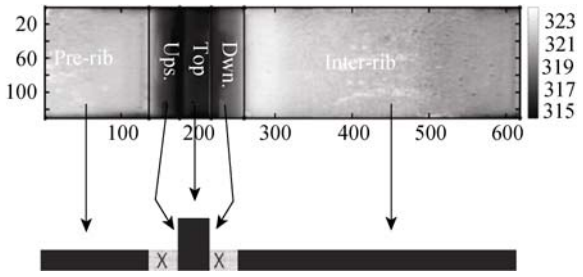

Fig. 5 Perspective Corrected Temperature [K]

The temperature data presented in Figure 5 has several limitations, one being the non-periodic temperature distribution in the rib domain. Specifically, this can be observed by the temperature distribution at the end of the pre-rib region not coinciding with the temperatures towards the end of the following inter-rib domain. The non-periodicity is evoked by several factors, such as the finite slab length (axial edge effects), heating of the bulk flow, and the aerodynamically non-fully-developed flow field. This would have been unproblematic if there existed surface temperature data for the entire test section, enabling formation of a finite element model over the complete slab to retrieve the local surface heat flux dis-

tributions. The issue arises since the surface temperature data exists for only a sector of the test section, hence a limited segment of the slab can be modeled numerically; but the necessary boundary conditions to impose on the transverse faces of the cut geometry are ambiguous. Imposing adiabatic boundary condition would be highly unrealistic considering that there are large local thermal gradients present within a rib passage. Furthermore, imposing periodicity boundary condition on a non-periodic temperature domain, results in superficial heat sources and sinks.

Thus, one of the reasonable approximations is to force temperature periodicity directly on the measured infrared data by linearly weighted (based on axial position) averaging of the overlap regions. This creates a realistic temperature distribution for a generic ribbed channel where periodicity holds. Finally, in order to reduce the noise content, a median filtering methodology is used. The temperature distribution across the channel is averaged with respect to the symmetry plane, followed by a Gaussian low pass filter to smooth out spuriously high gradients.

Surface Heat Flux Computation

To acquire the surface heat flux distribution, the bottom metallic wall of the test section is modeled by a finite element method solver, COMSOL. The commercial code solves the 3-D Fourier conduction equation throughout the model to compute the temperature distribution inside the solid body. The boundary conditions for the numerical 3-D conduction problem are uniform heat flux along the external surface, in this case 1733 W/m^2, measured temperature distribution on the top surface, adiabatic lateral walls and periodic boundary condition on the transverse direction where the solid, in reality, is interrupted, Fig. 6. The mesh consists of over 1.5E^6 tetrahedral elements with a maximum body and surface element size of 1mm and 0.1mm respectively.

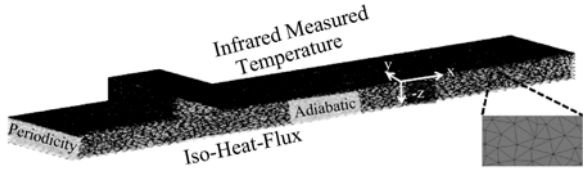

Fig. 6 Ribbed Slab FEM Model

Uncertainty Analysis

Performing experiments at the operational Reynolds number of 40,000, the uncertainty on Reynolds number, introduced by pressure and temperature measurements, is estimated as δRe/Re=3.3%. The overall uncertainty on infrared wall temperature measurements is δTwall=0.34°K. This results in a combined uncertainty in Nusselt number of δNu/Nu=3.7%.

Hotwire Anemometry

To supply complementary CFD simulations with appropriate aerodynamic inlet boundary conditions, hotwire anemometry measurements are conducted at the immediate upstream and downstream of the test section with smooth side walls. The test section inlet measurement plane is located 18.6 x/D$_h$ downstream of the channel leading edge, and the test section exit plane is 16.8 x/D$_h$ further downstream. At both axial positions the 75x 75mm square test section is divided into 3348 grid points such that 85% of the vertical direction (z-direction) and 100% of the horizontal direction (y-direction) has been resolved by a grid size of 1mm^2. The L-shaped hotwire is translated for the vertical and rotated for the horizontal motion. Hotwire anemometry data is acquired at 100kHz for one second duration at each grid point, and the resulting distributions are presented for channel Reynolds number of 40000.

The velocity profile is acquired by means of averaging the unsteady hotwire anemometry data at each grid point of the planar test section inlet and exit measurement locations. At both locations towards the channel walls, viscosity driven gradual decrease in mean flow velocity is observed, Fig. 7. Moreover, the symmetry plane velocity profile, is compared with the nth power law, $u/u_\infty = (2y/D_h)^{1/n}$, which is established for turbulent pipe flow. With n=6.6 at the investigated Reynolds number, a great similarity is observed between the empirical correlations and the experimental findings. The bulk velocity in the channel centerline is calculated to be 8.0 m/s, where as the passage average is 7.0 m/s.

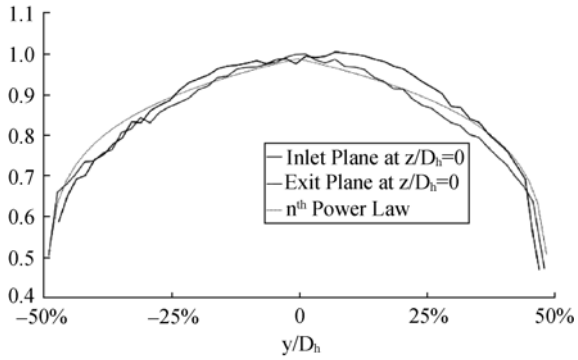

Fig. 7 Normalized Velocity Distribution

At the test section inlet and exit, the displacement thicknesses are calculated to be δ_{1i}=4.7mm and δ_{1e}= 5.5mm, where the growth is indicative of boundary layer

development; similar observations can be made for the momentum thicknesses, δ_{2i}=3.5mm and δ_{2e}=4.1mm. Shape factor, calculated by the ratio of the displacement and momentum thicknesses $H_{12}= \delta_1/ \delta_2$, is typically used for characterization of the state of the boundary layer. In this case, at both measurement planes, the shape factor is calculated to be in the order of H_{12}=1.33, consistent with fully turbulent boundary layer.

The time resolved velocity data enables the computation of turbulence intensity at a particular location, which is defined as the ratio of the perturbation root mean square with respect to the mean channel centerline velocity. The planar turbulence intensity distributions can be found in Fig. 8, where the channel averaged turbulence intensity is calculated to be 5.3% and 6.2% respectively at the inlet and exit. The clear quadrant symmetry is formed by the square geometry of the test section where the boundary layers from adjacent walls merge, creating low turbulence intensity regions in an X-pattern.

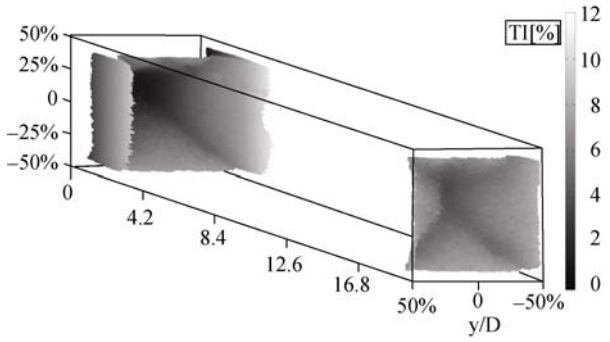

Fig. 8 Turbulence Intensity Distribution

The distribution of turbulence intensity across the channel can be explained by the existence of different regions in the turbulent boundary layer. The main force driving the free stream turbulence is associated with the eddies generated in the boundary layer. Towards the edges of the channel, around sub and buffer layers, the sharp decrease in turbulence intensity is due to relatively weak eddy shear stresses. Around the log-layer, a steep increase in turbulence intensity is detected; this is expected considering the large eddy shear forces at region of generation. Focusing towards the outer layer, as the inertial forces become more and more dominant, a gradual transition to free stream can be observed. At the geometric center of the channel, where turbulence intensity is low, the inertial forces are the dominant features of the local flow field. Towards the center of the inlet plane, the turbulence intensity is 1.6%, significantly less than the values observed further downstream, in the order of 4.1%. This may be indicative of inlet plane boundary layer eddies not penetrating as much to the channel core flow with respect to the exit plane.

The longitudinal augmentation in turbulence intensity, as well as the growth in displacement and the momentum thicknesses, is an indication of the not fully developed flow across the test section. Moreover, the mean ε dissipation rate across the channel is computed to be 8.5 Watts/kg and the related channel averaged Kolmogorov scale is 0.15mm.

Flat Plate Investigation

In order to verify the experimental conjugate heat transfer technique, as well as for conducting baseline investigations, the initial conjugate experiment is conducted on the flat plate geometry where uniform heat flux boundary condition is applied at the external side of the channel bottom wall. From a conjugate heat transfer perspective, such elementary geometries are crucial for comparison with purely convective iso-heat flux and iso-thermal wetted interface boundary conditions.

While the blower supplies the experimental rig with ambient temperature air for convection over the slab, the power supply connected to the Inconel foil is turned on, and the heat flux under the slab is gradually increased to 1167 W/m². Until steady-state conditions are reached, all temperatures along and under the slab, over the optical film and in the test section are monitored online and periodically. Once the test-section reaches steady conditions at Reynolds number 40000, 30 infrared images are acquired.

Then, the surface heat flux distribution of the wetted surface is acquired from the FEM solver. The local surface heat flux indicates that the conduction from bottom to top of the slab is not 1-D, and the error associated with such an assumption can be as high as 25% locally in the edges and in the order of 10% around the channel centerline. In the absence of a change in lateral conduction pattern, the change in normalized symmetry-line heat flux distribution can only be explained by axial conduction, in this case relatively small, in the order of 2.5%.

Nusselt Number Distributions

For parallel turbulent flow over a fully turbulent, no pressure gradient flat plate, with fixed aero and thermal boundary layer shapes, the corresponding iso-heatflux and iso-thermal interface boundary condition Nusselt number correlations are

$$Nu_x=0.0308Re_x^{4/5}Pr^{1/3} \quad (1)$$

and

$$Nu_x=0.0296Re_x^{4/5}Pr^{1/3} \quad (2)$$

respectively [7].

In the test case, the flow starts developing further upstream of the heated section, i.e. the aerodynamic boundary layer starts developing prior to its thermal counter-part. Its effect on local Nusselt number is rectified by an unheated entry length correction [8],

$$Nu_{x\xi}=Nu_x/(1-(\xi/x)^{9/10})^{1/9} \quad (3)$$

where ξ is the inlet unheated section length (1400mm) and x is calculated locally from the beginning of the inlet section. The wall of the unheated starting section, where $x < \xi$, is assumed to be at the same temperature as the air free-stream. Utilizing Eq. 1 and Eq.2 and by correcting for the unheated aerodynamic inlet length in Eq. 3, it is possible to acquire baseline Nusselt number distributions for purely convective heat transfer cases.

Figure 9 presents the experimental span-wise averaged conjugate Nusselt number distribution with error bars, along with the theoretical cases where the interface boundary condition is iso-heat-flux and isothermal. The longitudinal dimension is normalized by the local Reynolds number, with length scales measured in reference to the heated slab leading edge. In all three cases, due to thermal boundary layer development, there is a monotonous decrease in Nusselt number at increased axial position.

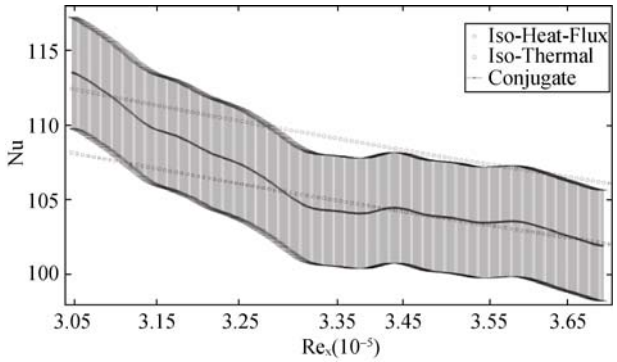

Figure 9 Conjugate Flat Plate - Widthwise Averaged Nusselt number

The isothermal boundary condition case is a lower bound on heat transfer since, as the thermal boundary layer develops, the descended layers of fluid at the adjoining wall come into contact with closer solid temperatures, decreased temperature head, resulting in reduced heat flux. As less work is done on the local thermal boundary layer, the cross-sectional temperature gradients near the wall reduce in the downstream direction, yielding lessened heat transfer. In contrast, for the iso-heat-flux case, an equal amount of work is inflicted on the thermal boundary layer, independent of local heat transfer coefficient.

In the conjugate case, in addition to the adverse effects of thermal boundary layer development on Nusselt number, the conduction within the solid has also an impact on local heat transfer. On one hand, the axial conduction within the solid in the flow upstream direction ensures more than isothermal local heat flux. But, on the other hand, since the solid can't sustain as large thermal gradients as the iso-heat-flux boundary condition, the resultant conjugate heat transfer is less than this limit. It is important to note that, within the uncertainty, the experimental conjugate results are in between the two limiting cases, consistent with theory which states that the iso-heat flux boundary condition is an upper bound on the iso-thermal interface boundary condition, and all conjugate Nusselt number distributions must lay within these two limits [9].

Overall, the selection of conjugate boundary condition over the convective counter parts has a relatively small effect on Nusselt number, in the order of 3%; expected considering the turbulent flow and at relatively high Reynolds number over a flat plate [10]. Comparing the findings with the analytical conjugate heat transfer investigations [11], similar observations can be made. Defining a local Brun number

$$Br_x=(d/x)\ K^{-1}\ (Pr\ Re_x)^{1/3} \quad (4)$$

yields Br_x= 0.06 for the conjugate flat plate. From Ref. [11], the conjugate deviation from the isothermal boundary condition is given by,

$$X=1-2.98\ \phi_w/((1-\phi_w)\ Br_x) \quad (5)$$

where $\phi_w=1/(1-2In(\phi_w)+8.89/Br_x^2)^{0.5}$, which is the relative temperature drop across the plate thickness with respect to the plate external side temperature difference from the bulk flow. In this case, the computed ϕ_w=0.02, and the subsequent deviation of the conjugate boundary condition case from its iso-thermal counterpart is X=2%, consistent with the findings in Figure 9.

Ribbed Channel Investigation

In order to quantify the effects of conduction in convective heat transfer for geometries where local protrusions are present, similar infrared thermography investigations are conducted for the ribbed slab configuration.

Applying the measured surface temperature distribution to Comsol as a boundary condition, it is possible to acquire the heat flux distribution within the solid, as presented in Figure 10. It is important to point out that there exists large heat flux redistribution in the metallic domain, an artifact of the solid conduction. This effect is observed to be especially dominant in the vicinity of the rib which creates a local heat sink, Figure 10.

With the local temperature and the surface heat flux, it is possible to calculate Nusselt number distributions over the wetted surface. In order to quantitatively assess the impact of artificial roughness elements on internal cooling channels and thus determine the relative heat transfer enhancement, the Nusselt number is normalized by the Dittus Boelter flat plate heat transfer correlation (Nu_o) with the new parameter referred to as enhancement factor (EF).

Figure 11 illustrates the enhancement factor distributions over the test section. Considering the insight about the flow structures which Particle Image Velocimetry experiments of Casarsa [5] provide, it is possible to iden-

tify some unique distributions of enhancement factor associated with the nearby flow features. On the upper half of Figure 11 are the surface streamlines superimposed from Ref. [5]. The schematics denoted on the side of the figure are the V_3, V_2 and V_1 vortex structures, located in front of, over, and behind the rib respectively, observed around the channel symmetry line.

Entering the ribbed test section from the left hand side, $-6<x/H<-3.8$, the flow through the inter-rib spacing reattaches and aligns with the passage successional to the rib downstream recirculation region. The progressive decrease in enhancement factor in the region further downstream, $-3.8<x/H<-1.5$, is attributed to a redeveloping boundary layer.

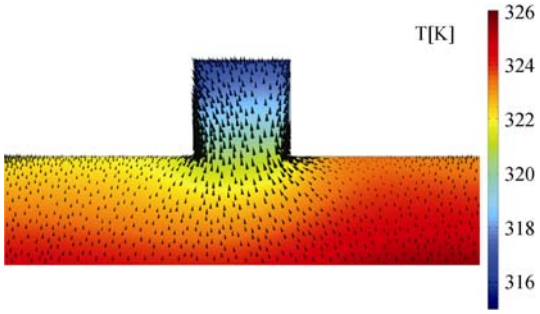

Fig. 10 Solid Heat Flux Distribution around the Rib

In Figure 11, the upstream rib face is denoted by the $-1.5<x/H<-0.5$ domain. As the mainstream flow approaches the turbulator, $-1.5<x/H<-0.8$, the characteristic flow structure V_3, situated immediately upstream, induces a noticeable blockage effect which prevents the cool bulk flow to come in contact with the lower portion of the rib upstream surface. This is evident by the low enhancement factor developing in the corner region. Above this V_3 covered portion, strong flow impingement on the front surface of the rib is indicated by the peak in enhancement factor observed at around $x/H=-0.8$.

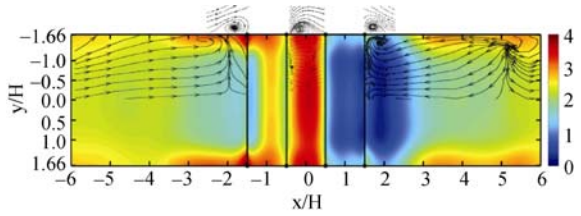

Fig. 11 EF at the Projected Boundary

The overall highest EFs are observed at the top face of the rib, $-0.5<x/H<0.5$. Here, as induced by the strong flow deviation imposed by the turbulator and the decrease in effective passage cross section, a region of locally augmented heat transfer is created in the presence of high momentum flow. A gradual widening of the local EF peak can be seen towards the lateral wall which is in agreement with the larger, more diffuse, vortex formation V_2.

The downstream surface of the rib, $0.5<x/H<1.5$, along with the immediate downstream in the axial direction, $1.5<x/H<2$, are the regions where the lowest EF values are observed. This is attributed to the presence of the recirculation bubble governing the rib downstream region. Resulting in a region of local low momentum and reversed flow, the heat transfer in this area is considerably decreased when compared to the rest of the passage. In addition to the global separation, there is the existence of a counter clockwise rotating vortex V_1, further isolating the region from the mainstream flow, $0.9<x/H<1.5$. The rise in EF in streamwise direction, $1.5<x/H<6$, is induced by increased influence of cool mainstream flow within the separation bubble, at regions further away from the rib.

Overall, the average EF on the upstream rib face is relatively high, 2.34, due to the impingement of the mainstream flow on the surface. On the rib top face, the EF is even further augmented, 2.99, due to the local increase of momentum by the decrease in effective area. On the downstream side of the rib, the lowest average EF is observed, 0.86, due to the large separated region behind the step. The rib, inter-rib and domain averaged EFs are 2.07, 2.01 and 2.02 respectively.

Comparison with Literature

Figure 12 presents the comparison of the findings on the channel symmetry line with respect to similar studies conducted in prior literature. The convective liquid crystal data are the results gathered by Cakan [12] in his experiments conducted with the iso-heat-flux boundary condition at Re=30000. The "LES" data is from an internal study at VKI, based on the current conjugate test case [13]. Agostini et. al. conducted similar conjugate heat transfer experiments in a ribbed channel [14]. All test cases show remarkable resemblance to the current experimental data set.

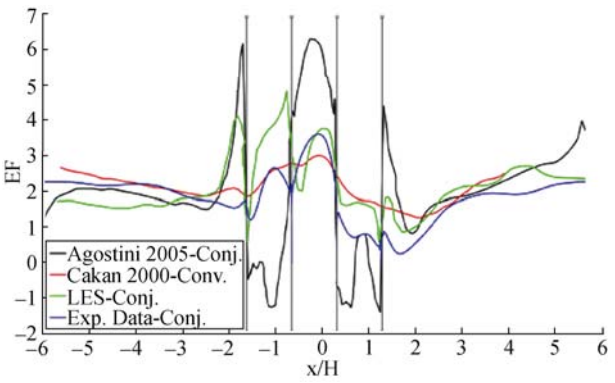

Fig. 12 Symmetry Line EF Comparison

By comparing the convective case study [12] with its conjugate counterparts in Figure 12, there appears to be a high degree of consistency in the inter-rib spacing. However, the spread of enhancement factor in the vicinity of the rib, $|x/H|<3$, is evident. This is an indication of the heat transfer levels being highly influenced by the imposed boundary condition near geometric externalities. It is believed to be attributed to the dominant conduction coupling, particularly observed in proximity of the rib as a result of closely distributed local heat sinks and sources. Alternatively, considering the criteria outlined in Ref. [11], using the characteristic length associated with rib height, the local Brun number can be estimated as 0.17. Greater than 0.1, the conduction-convection coupling effects are demonstrated to be non-negligible.

Conclusions

In order to characterize the test section inlet flow, as well as to provide appropriate aerodynamic inlet boundary conditions to complementary CFD simulations, hot-wire anemometry measurements are conducted at the immediate upstream and downstream of the test section with smooth side walls.

In aero-thermal investigations, a test section is constructed to quantify to underlying physics of the conjugate heat transfer, where the heat flux is imposed at the external bottom side of the test section. To calculate local heat flux, the Infrared Thermography measured temperatures are imposed as boundary conditions on the finite element model. The simple ribbed and flat plate configurations of the conjugate test cases create an opportunity to establish fundamental baseline experimental studies, not only applicable in turbomachinery but of much broader interest.

For the conjugate flat plate experiments, the experimental Nusselt number distribution, along with analytical solutions indicated that the effect of non-isothermal (conjugate) boundary condition is estimated to be in the order of 3%. Even for the experiments conducted for a flat plate geometry, the local heat-flux distribution seems to be influenced by the existence of the slab and thus the conduction effects. However, lacking strong spatial thermal gradients, the mean heat transfer does not seem to be as susceptible to the conjugate phenomena for this configuration.

For the ribbed channel, the heat transfer distributions are normalized by enhancement factor and the trends are compared with the basic flow features observed in prior literature and reflected excellent agreement. Comparing the conjugate ribbed slab enhancement factor with conjugate and convective literature, a high degree of overall correlation is evident. Moreover, the conduction-convection coupling effects are demonstrated to be non-negligible, which is an indication of the heat transfer being influenced by the imposed boundary condition.

Acknowledgement

The authors acknowledge the financial support of the Air Force Office of Scientific Research (AFOSR), Grant FA8655-08-1-3048, supervised by Dr. S. Surampudi and Dr. G. Abate of the European Office of Aerospace Research and Development.

References

[1] Perelman, L.T.: On Conjugated Problems of Heat Transfer, International Journal of Heat and Mass Transfer, vol.3, no.4, pp.293–303, (1961).

[2] Dorfman, A.; Renner, Z.: Conjugate problems in Convective Heat Transfer: Review, Mathematical Problems in Engineering, Article ID 927350, (2009).

[3] Luikov, A.V.; Aleksachenko, A.A.: Analytical Methods of Solution of Conjugate Problems in Convective Heat Transfer, International Journal of Heat and Mass Transfer, vol.14, no.8, pp.1047–1056, (1971).

[4] Luikov, A.V.: Conjugate Convective Heat Transfer Problems, International Journal of Heat and Mass Transfer, vol.17, no.2, pp.257–265, (1974).

[5] Casarsa, L.: Experimental Investigation of the Aerothermal Performance of a High Blockage Rib-roughened Cooling Channel, ASME Journal of Turbomachinery, vol.127, pp.580–588, (2005).

[6] Rau, G.; Moeller, D.; Cakan, M.; Arts, T.: The Effect of Periodic Ribs on the Local Aerodynamic and Heat Transfer Performance of a Straight Cooling Channel, ASME Journal of Turbomachinery, 120, 1998, 268–275.

[7] Kays, W.; Crawford, M.; Weigand, B.: Convective Heat and Mass Transfer, McGraw-Hill, New York, ISBN 0-072-99073-2, 2005.

[8] Incropera, F.P.; DeWitt, D.P.: Fundamentals of Heat and Mass Transfer, John Wiley & Sons, Inc., New Jersey, ISBN 0-471-38650-2, (2000).

[9] Mori, S.; Sakakibara, M.; Tanimoto, A.: Steady Heat Transfer to Laminar Flow in a Circular Tube with Conduction in the Tube Wall, Heat Transfer - Japanese research, vol.3, no.2, pp.37–46, (1974).

[10] Dorfman, A.: Conjugate Problems in Convective Heat Transfer, Taylor & Francis, London, UK, ISBN 1-420-08237-X, (2009).

[11] Mosaad, A.: Laminar Forced Convection Conjugate Heat Transfer over a Flat Plate, Heat and Mass Transfer, vol.35, no.5, pp.371–375, (1999).

[12] Cakan, M.: Aero-Thermal Investigation of Fixed Rib-Roughened Internal Cooling Passages, Ph.D. thesis, Université catholique de Louvain, Louvain, Belgium, (2000).

[13] Benocci, C., Internal Communications in von Karman Institute for Fluid Dynamics, Brussels, PR 2008-18, (2008).

[14] Agostini, F.; Arts, T.: Conjugate Heat Transfer Investigation of Rib-Roughened Cooling Channels, ASME Turbo Expo 2005, Reno, Nevada, (2005).